PAPER

Check for updates

Bifunctional 2D-on-2D MoO₃ nanobelt/Ni(OH)₂ nanosheets for supercapacitor-driven electrochromic energy storage†

Liangliang Zhu,[a] Connor Kang Nuo Peh,[a] Ting Zhu,[a] Yee-Fun Lim [iD] [b] and Ghim Wei Ho [iD] *[abc]

A hybrid composite that unifies multiple structural attributes is the key for improved functional device performance. Moreover, hierarchical and porous assembly of dissimilar constituent elements at various length scales and dimensionality is highly appropriate for mass transfer and surface/interfacial-dominated reactions. Here, we demonstrate solution processed 2D-on-2D hierarchical architecture of nanobelt core–nanosheets shell consisting of dissimilar transition metal composite. The defining benefits of such hetero-structured material design are short ion diffusion pathway of a thin 2D nanobelt core that is interfaced to large surface area and porous 2D nanosheets. Accordingly, an integrated energy system that delivers multiple functionalities, *i.e.* supercapacitive charge storage and electrochromic optical modulation, is investigated due to its attractive complementary energy storage and energy conservation capabilities. Consequently, bifunctional electrochromism–supercapacitive properties are demonstrated where desirable optical transmittance modulation and coloration efficiency properties in parallel with favorable pseudocapacitive storage and specific capacitance properties are simultaneously realized. Such an integrated energy system is anticipated to have a broad range of smart applications in buildings, automobiles and other emerging electronics needs.

Introduction

Design of nanomaterial of dissimilar composition and structure presents potential synergistic effects between different material constituents and dimensionality for improved device performance.[1–5] Moreover, rational hierarchical and porous structural design can lead to superior physicochemical properties beneficial for various mass transfer and surface/interfacial-dominated reactions.[6–8] On the contrary, aggregated and non-porous materials generally grant limited accessibility to the surface owing to restricted contact of only the outermost material with reactants. Besides, it is well known that a 2D nanostructure which is largely made up of surface atoms with highly exposed surfaces is the ideal morphological basis for surface/interfacial-dependent electrochemical reactions.[9,10] 2D nanostructures, in particular transition metal oxides and hydroxides, are well suited for electrochemical studies since most of them possess not only multiple

oxidation states but also layered crystal structures that favor reversible intercalation reactions.[11–13]

Electrochemical-based phenomena, *i.e.* supercapacitive charge storage and electrochromic optical modulation, have garnered immense attention due to their corresponding attractive energy storage and energy conservation capabilities.[14,15] In prior works, electrochromic materials were mostly studied with external powering batteries without considering deployment or reutilization of the energy stored in these electrochromic materials for useful purposes.[16,17] However, with increasing interest in integrated energy systems that can deliver multiple functionalities, it is appealing to adopt electrochromism and supercapacitive capabilities into an integrated system. The associated mechanisms are highly compatible in operation since some of the electrochemically active materials exhibit charge insertion/extraction or chemical reduction/oxidation processes that are accompanied by reversible change of colors.[18,19] Despite rapid advancement in the independent research on supercapacitor and electrochromic nanomaterials, there is limited work on completely solution-processed 2D hetero-structured transition metal materials with hierarchical porous architecture that exhibit complementary capacitive storage and chromogenic capabilities. Presumably the challenges lie in the difficulties in controlling different growth mechanisms and in regulating growth dynamics of disparate material systems into an appropriate design framework.

[a]*Department of Electrical and Computer Engineering, National University of Singapore, 4 Engineering Drive 3, Singapore 117583. E-mail: elehgw@nus.edu.sg*

[b]*Institute of Materials Research and Engineering, A*STAR (Agency for Science, Technology and Research), 3 Research Link, Singapore 117602*

[c]*Engineering Science Programme, National University of Singapore, 9 Engineering Drive 1, Singapore 117575*

† Electronic supplementary information (ESI) available: Additional SEM, TEM, XRD, FTIR and photographs. Specific capacitances and cycling performances of the material. See DOI: 10.1039/c7ta01858d

This journal is © The Royal Society of Chemistry 2017

J. Mater. Chem. A, 2017, **5**, 8343–8351 | 8343

Herein, we synthesize a 2D-on-2D hierarchical architecture of nanobelt core–nanosheets shell of disparate transition metal composite based completely on the solution processing method. The growth of 2D $Ni(OH)_2$ nanosheets on free-standing 2D MoO_3 nanobelts manifests in a 3D hierarchical architecture of numerous nanosheets that extend radially outward. The defining advantages of such hetero-structured material design are short ion diffusion pathway of the 2D thin nanobelt core that interfaces with large surface area and interconnected porous 2D nanosheets.[20] Accordingly, bifunctional electrochromism–supercapacitive application is demonstrated based on the inexpensive electrochemical active transition metal hydroxide/oxide hierarchical structure. The porous core–shell nanostructures of $Ni(OH)_2/MoO_3$ display desirable electrochromic optical modulation and coloration efficiency properties alongside favorable pseudocapacitive storage and specific capacitance properties. The high rate capacity for complementary energy storage and optical modulation capabilities can be attributed to the beneficial structural features of the hybrid metal oxide–metal hydroxide composition and nanobelt backbone core that supports large surface area electrochemically active nanosheets. To this end, bifunctional electrochromic and supercapacitive materials are anticipated to have a broad range of energy applications in smart windows, displays, automobiles and various intelligent electronics.

Experimental section

Synthesis of single crystal MoO_3 nanobelts

In a typical procedure, a certain amount of sodium molybdate ($Na_2MoO_4 \cdot 2H_2O$) was dissolved into 25 ml deionized water to form a 0.1 mol L^{-1} solution. The pH of the $Na_2MoO_4 \cdot 2H_2O$ solution was adjusted to be 1.5 using hydrochloric acid (HCl, 37–38 wt%). After that, the solution was transferred into a 50 ml Teflon-lined stainless steel autoclave and was heated at 180 °C for 10 hours. After hydrothermal treatment, the autoclave was cooled down to room temperature. Subsequently, the precipitates were separated and washed with deionized water by centrifugation 3 times. Finally, the products were dried in vacuum at 60 °C for 2 hours.

Synthesis of $MoO_3/Ni(OH)_2$

5 mg as-prepared MoO_3 nanobelts were dispersed in 30 ml absolute ethanol. After sonication for a few minutes, 0.0727 g nickel nitrate hexahydrate ($Ni(NO_3)_2 \cdot 6H_2O$) and 0.28 g hexamethylenetetramine were added to the suspension. The hydrothermal treatment was subsequently conducted at 120 °C for 4 hours. After the reactions, the products were washed with ethanol and dried at 55 °C.

Characterizations

Crystallographic information about the fabricated products was obtained using X-ray diffraction (XRD, Bruker D5005 X-ray diffractometer with Cu Kα radiation at $\lambda = 1.541$ Å). Morphology and structural characteristics were studied using field-emission scanning electron microscopy (SEM, JEOL FEG

JSM 7001F). The elements were analyzed by energy-dispersive X-ray spectroscopy (EDX, Oxford Instruments). The crystal structure of the composite was investigated by using transmission electron microscopy (TEM, Philips FEG CM300) at 200 kV, and X-ray photoelectron spectroscopy (XPS, VG Thermo Escalab 220I-XL). Fourier transform infrared (FT-IR) spectra were recorded with a Shimadzu IR Prestige-21 FT-IR spectrophotometer. Brunauer–Emmett–Teller (Quantachrome Nova 2200) measurements were conducted with nitrogen (N_2) as the adsorbate at liquid nitrogen temperature.

Electrochemical measurements

The working electrodes were prepared by mixing 70 wt% of electroactive material ($MoO_3/Ni(OH)_2$ and pure $Ni(OH)_2$ nanosheets), 20 wt% of carbon black, and 10 wt% of polyvinylidene difluoride (Aldrich). The slurry was then pressed onto Ni metal foams, and dried thoroughly at 55 °C. The electrolyte used was a 3 M potassium hydroxide (KOH) aqueous solution. The electrochemical performances including CV, GCCD and EIS (frequency ranging from 0.01 to 100 kHz with 5 mV amplitude) of the individual electrodes were evaluated with a CHI660e electrochemical workstation using cyclic voltammetry and chronopotentiometry tests with a three-electrode cell where Pt foil served as the counter electrode and a standard calomel electrode (SCE) as the reference electrode.

Assembly of $MoO_3/Ni(OH)_2$ asymmetrical supercapacitors

Asymmetrical supercapacitor full cells (5 cm × 4 cm) were assembled using two pieces of nickel foam loaded with $MoO_3/Ni(OH)_2$ and carbon nanotubes (CNTs), respectively. The two electrodes were packed with Al foil using an electrolyte-soaked (3 M KOH) separator in between. The mass of the active materials in the two electrodes was calculated beforehand based on the charge balance to maximize the energy density of the cells.

Electrochromic measurements

The $MoO_3/Ni(OH)_2$ composite was dispersed in glycol and spin-coated onto fluorine-doped tin oxide (FTO) glass. The coated FTO glass was then dried at 55 °C for 3 h. The sample (working electrode) was placed in 1 M KOH electrolyte solution and a Pt foil was used as the counter electrode. A forward voltage bias was applied to induce a color change in the $MoO_3/Ni(OH)_2$ coating and a reverse bias was applied to bleach the electrochromic layer. The absorption and transmittance spectra of the samples were measured with a UV-VIS-NIR spectrophotometer (Shimadzu UV-3600). Real time transmittance measurement was carried out with a spectrophotometer (Ocean Optics Maya2000 Pro) and a 500 nm light emitting diode (LED) was used as the light source. Based on setting the transmittance of the bleached state as ca. 90%, each bias state was maintained for 10 s before switching to the opposite polarity.

Electrochromic storage device measurements

Three coated FTO glasses were connected in series. A +2 V voltage was applied to drive the electrochromic reaction. After

the glasses turned black, a green LED was connected in the circuit and it lit up.

Results and discussion

2D MoO_3 nanobelts and secondary outerlying 2D $Ni(OH)_2$ nanosheets were fabricated successfully by facile hydrothermal and solvothermal methods, respectively.[21,22] A schematic illustration is shown in Fig. 1a. The morphology and structure of MoO_3 nanobelt and $Ni(OH)_2/MoO_3$ were first characterized by SEM, as shown in Fig. 1b–g. The smooth MoO_3 nanobelt structures with an average width of 150 nm (Fig. 1b and c) and thickness of *ca.* 30 nm (Fig. 1d) can be clearly observed. Using the MoO_3 nanobelts as a nucleation platform, $Ni(OH)_2$ nanosheets could be uniformly grown solvothermally. The $Ni(OH)_2$ nanosheets distributed on the surface of the MoO_3 nanobelts and thus formed a 2D-on-2D hierarchical architecture of nanobelt core–nanosheets shell (Fig. 1e–g). The TEM images of MoO_3 nanobelts show that the distances of lattice strips are about 0.40 nm and 0.37 nm, corresponding to the (100) and (001) planes of the orthorhombic α-MoO_3 phase (Fig. 2a and b).[23,24] The selected area electron diffraction pattern recorded perpendicular to the growth axis of a single nanobelt (Fig. 2c) could be attributed to the [010] zone axis diffraction of single-crystalline α-MoO_3, and suggested that the nanobelt grew along the [001] direction.[25–27] A clear core/shell structure of $MoO_3/Ni(OH)_2$ is illustrated in the TEM image (Fig. 2d). An interplanar spacing of 0.27 nm in outer thin nanosheets (Fig. 2e) corresponds to the (100) planes of $Ni(OH)_2$ (Fig. 2e, inset).[28] Elemental mapping was also performed to better illustrate the core/shell structure. As shown in Fig. 2f, the nanobelt core of MoO_3 inside is revealed by the Mo element mapping, covered by a uniform sheath consisting of Ni and O elements.

The crystal structures of MoO_3 nanobelts and $MoO_3/Ni(OH)_2$ were also investigated by XRD and the spectra are shown in Fig. 2g. XRD perfectly assigned to orthorhombic α-MoO_3 (JCPDS card no. 05-0508) in accordance with the results of TEM analysis, which is the conventional thermodynamically stable phase. The absence of noticeable impurity peaks suggests the high purity of the α-MoO_3 product. The stronger intensities of the (020), (040), and (060) diffraction peaks suggest highly anisotropic growth of the nanostructures.[26] The structure of α-MoO_3 is shown in Fig. 2g (inset, upper), which is constituted of [MoO_6] octahedra, with sharing edges and corners, resulting in zigzag chains and unique layer parallel to the (010) plane structure, presenting open channels for H^+ ion intercalation.[29] After growth of $Ni(OH)_2$ nanosheets, the enhanced peaks located at 33° and 59° can be indexed to (110) and (300) crystal planes of α-$Ni(OH)_2$ (JCPDS card no. 22-0444), the crystalline structure of which is illustrated in Fig. 2g (inset, lower). The XRD spectrum of pure $Ni(OH)_2$ nanosheets (morphology and structure are illustrated in Fig. S1 and S2†) synthesized in the absence of MoO_3 nanobelts under the same conditions further
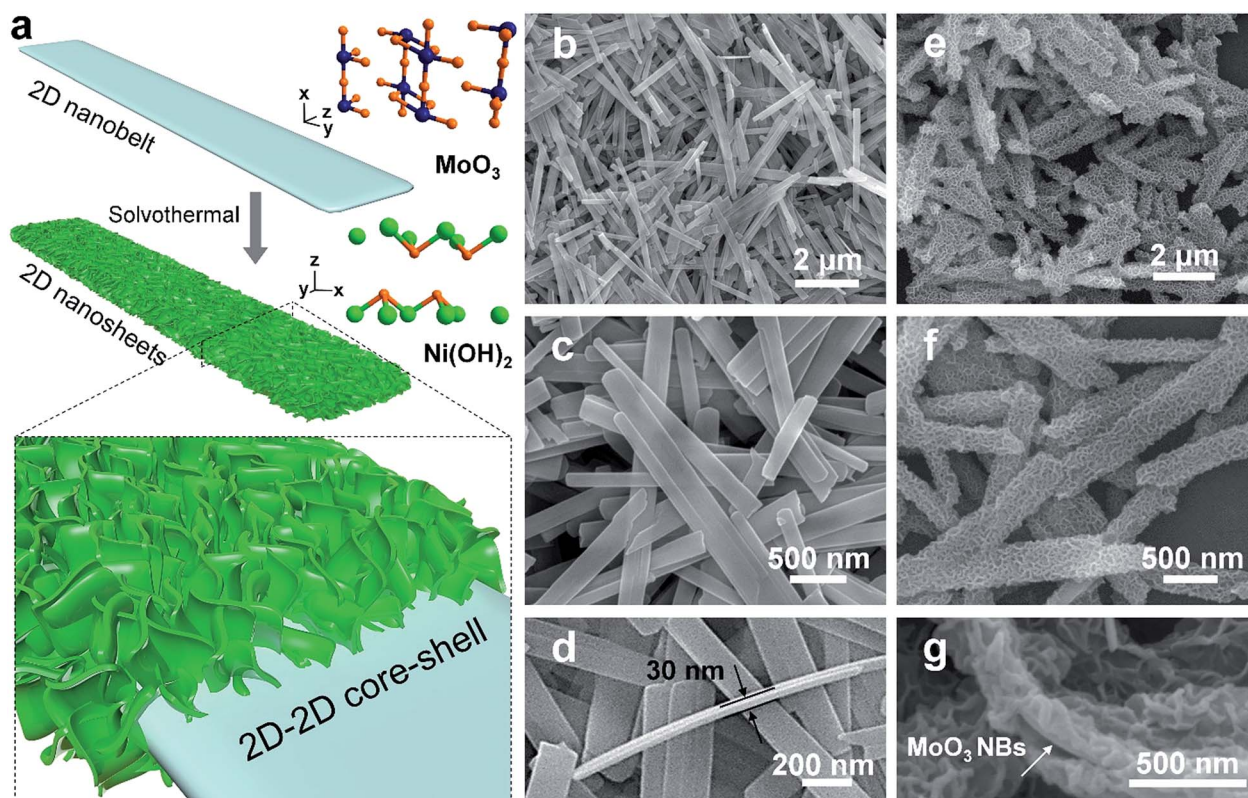
Fig. 1 (a) Schematic illustration of synthesis of 2D-on-2D $MoO_3/Ni(OH)_2$. (b–d) SEM images of MoO_3 nanobelts. (e–g) SEM images of $MoO_3/Ni(OH)_2$.

This journal is © The Royal Society of Chemistry 2017
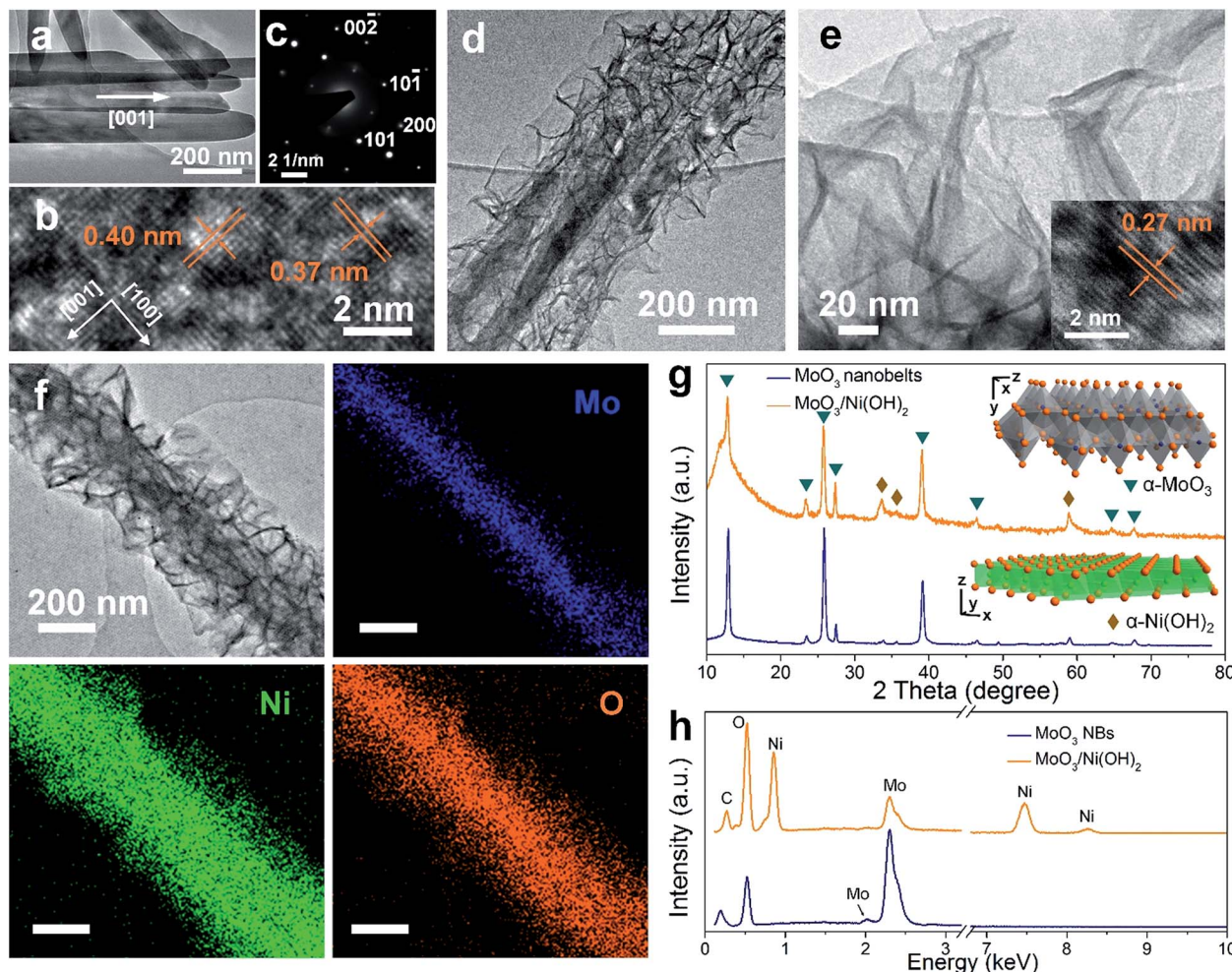
J. Mater. Chem. A, 2017, **5**, 8343–8351 | **8345**

Fig. 2 TEM images of MoO_3 nanobelts at (a) low and (b) high resolution. (c) Selected area diffraction pattern. (d and e) TEM images of MoO_3/$Ni(OH)_2$; inset: TEM image of outerlying $Ni(OH)_2$ nanosheets at high resolution. (f) Elemental mapping images of MoO_3/$Ni(OH)_2$ (the scale bar is 200 nm). (g) XRD spectra of MoO_3 nanobelts and MoO_3/$Ni(OH)_2$; insets: schematic representation of α-MoO_3 (upper) and α-$Ni(OH)_2$ (lower) crystalline structures. (h) EDX spectra of MoO_3 nanobelts and MoO_3/$Ni(OH)_2$.

indicates the α-$Ni(OH)_2$ phase, as shown in Fig. S3.†[30] The EDX spectra of both MoO_3 nanobelts and MoO_3/$Ni(OH)_2$ in Fig. 2h show C, O and Mo peaks at 0.26 keV, 0.52 keV, 2.02 keV and 2.30 keV, corresponding to the composition of MoO_3 nanobelts. Ni peaks are seen at 0.85, 7.47 and 8.25 keV in MoO_3/$Ni(OH)_2$, indicating the growth of $Ni(OH)_2$ nanosheets.[23,31] The chemical compositions of MoO_3 nanobelts and MoO_3/$Ni(OH)_2$ were also confirmed by FT-IR spectra, shown in Fig. S4.† The bands appearing at approximately 3600–3000, 1700–1400, 1380, 1300–1000 and 1000–800 cm^{-1} can be assigned to the characteristic vibrations of O–H stretching, O–H bending, NO_3^- anions, C–O stretching and Mo–O_2 stretching, Mo–O–Mo bridge stretching.[32] The peak at 610 cm^{-1} can be assigned to the Ni–O, O–Ni–O, and Ni–O–Ni vibrations.[30]

XPS analysis was adopted to determine the chemical states of the MoO_3 nanobelts and MoO_3/$Ni(OH)_2$, particularly for Mo, O and Ni. The wide scan spectrum in Fig. 3a shows the binding energy peaks at 285.0 and 530.1 eV, which are attributed to C 1s and O 1s, respectively. Binding energies of 232.6 and 235.8 eV are indicative of Mo $3d_{5/2}$ and Mo $3d_{3/2}$, with the Mo 3d

spectrum (Fig. 3b) corresponding to the Mo^{6+}.[27] Meanwhile, a slight shift and FWHM broadening of the peaks of Mo 3d and O 1s for MoO_3/$Ni(OH)_2$ could be ascribed to the growth of $Ni(OH)_2$ nanosheets. A shoulder peak appearing at 532.6 eV (Fig. 3c, MoO_3/$Ni(OH)_2$) is attributed to the interstitial oxygen or the chemisorbed oxygen atoms on the surface of MoO_3.[33] The Ni 2p peak is shown in Fig. 3d. The Ni $2p_{3/2}$ peak is located at 855.6 eV with a shakeup satellite peak at about 861.2 eV and Ni $2p_{1/2}$ at 873.2 eV with a shakeup satellite peak at about 879.2 eV, which correspond to Ni^{II}.[34,35] The gap between Ni $2p_{3/2}$ and Ni $2p_{1/2}$ is about 17.6 eV, which is in agreement with previous reports.[36] N_2 adsorption–desorption measurements obtained from MoO_3/$Ni(OH)_2$ and pure $Ni(OH)_2$ nanosheets gave specific surface areas of 152.6 and 148.2 m^2 g^{-1} and a similar pore size distribution of ~2 nm, as shown in Fig. 3e and f, respectively.

The as-prepared MoO_3/$Ni(OH)_2$ and pure $Ni(OH)_2$ nanosheets were evaluated as electrodes for supercapacitors. Fig. 4a shows the cyclic voltammetry (CV) curves obtained from different scan rates (1–20 mV s^{-1}) with a voltage window of 0–0.6 V (*vs.* SCE) for pure $Ni(OH)_2$ nanosheets and MoO_3/$Ni(OH)_2$.

8346 | *J. Mater. Chem. A*, 2017, 5, 8343–8351

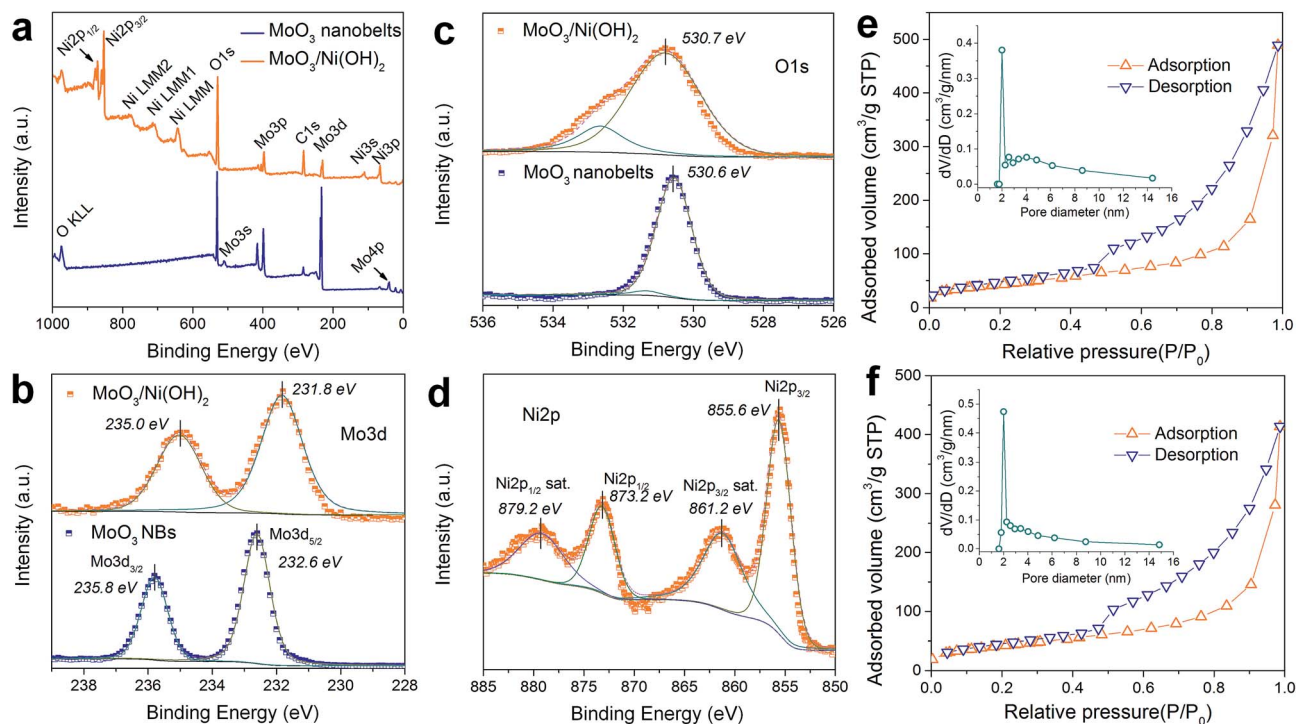This journal is © The Royal Society of Chemistry 2017

Fig. 3 (a) XPS spectra of MoO_3 nanobelts and $MoO_3/Ni(OH)_2$. (b–d) High-resolution XPS spectra of MoO_3 nanobelts and $MoO_3/Ni(OH)_2$ for (b) Mo 3d, (c) O 1s and (d) Ni 2p. N_2 absorption and desorption isotherm linear plots of (e) $MoO_3/Ni(OH)_2$ nanosheets and (f) pure $Ni(OH)_2$; the insets show the corresponding pore size distributions.

A pair of redox peaks is observed in each curve suggesting that measured capacitance is mainly based on the pseudocapacitive mechanism. The intensities of the redox peaks increase and the cathodic peak is shifted to the positive direction while the anodic peak is shifted to the negative direction with scan rate, further confirming the pseudocapacitive property of the material.[37,38] The average specific capacitances of the samples can be calculated from the CV curves based on the following equation:[39]

$$C = \frac{1}{mu(V_2 - V_1)} \int_{V_1}^{V_2} I(V)\mathrm{d}V \qquad (1)$$

where C (F g^{-1}) is the specific capacitance, m (g) is the mass of the active material, I (A) is the current, u (V s^{-1}) is the CV scan rate, and V_1 and V_2 (V) are the voltage cuts during the CV scanning.

The average specific capacitances of the two samples calculated from different scan rates are displayed in Fig. 4a and b. Specific capacitances of 1510, 1455, 1142, 736, and 358 F g^{-1} can be calculated at scan rates of 1, 2, 5, 10 and 20 mV s^{-1} for $MoO_3/Ni(OH)_2$, which are higher than those of pure $Ni(OH)_2$ except at the rate of 20 mV s^{-1} (Fig. 4c). The specific capacitances were also determined by galvanostatic charge–discharge (GCD) measurements at various current densities at room temperature and calculated by the following equation:[40]

$$C = \frac{I\Delta t}{m\Delta V} \qquad (2)$$

where I (A) is the discharging current, Δt (s) is the discharging time, m (g) is the weight of materials and ΔV (V) is the voltage interval of the discharge. As shown in Fig. 4d and e, the calculated capacitances are 1622, 1425, 1163 and 418 F g^{-1} for $MoO_3/Ni(OH)_2$ and 940, 898, 840 and 660 F g^{-1} for pure $Ni(OH)_2$ nanosheets at current densities of 1, 2, 5 and 10 A g^{-1} (Fig. S5†), which are consistent with the CV scanning results.

Furthermore, the cyclic stability of the electrode materials is another key issue for practical application; therefore, the GCD test was performed to evaluate the stability of the electrode at a current density of 5 A g^{-1}. As shown in Fig. S6,† the electrode exhibits good long-term cyclic stability, maintaining 80% of its original capacitance (a decrease from 1150 to 921 F g^{-1}) after 3000 cycles. The electrochemical impedance spectroscopy (EIS) analyses of $MoO_3/Ni(OH)_2$ and pure $Ni(OH)_2$ nanosheets in the frequency range from 0.01 to 100 kHz are shown as Nyquist plots in Fig. 4f. The equivalent series resistance was only 1.71 Ω in the high-frequency region, which is lower than that of pure $Ni(OH)_2$ nanosheets. The semicircles crossing high and mid-frequencies are attributed to the charge-transfer resistance, which has been enlarged and shown in the inset of Fig. 4f. The lower equivalent series resistance together with the smaller radius of charge-transfer resistance can generally indicate a lower impedance and better electric conductivity for $MoO_3/Ni(OH)_2$, which could lead to a better electrochemical performance.

α-$Ni(OH)_2$ is an excellent anodic electrochromic material and can change color upon OH$^-$ ion insertion due to its isostructure
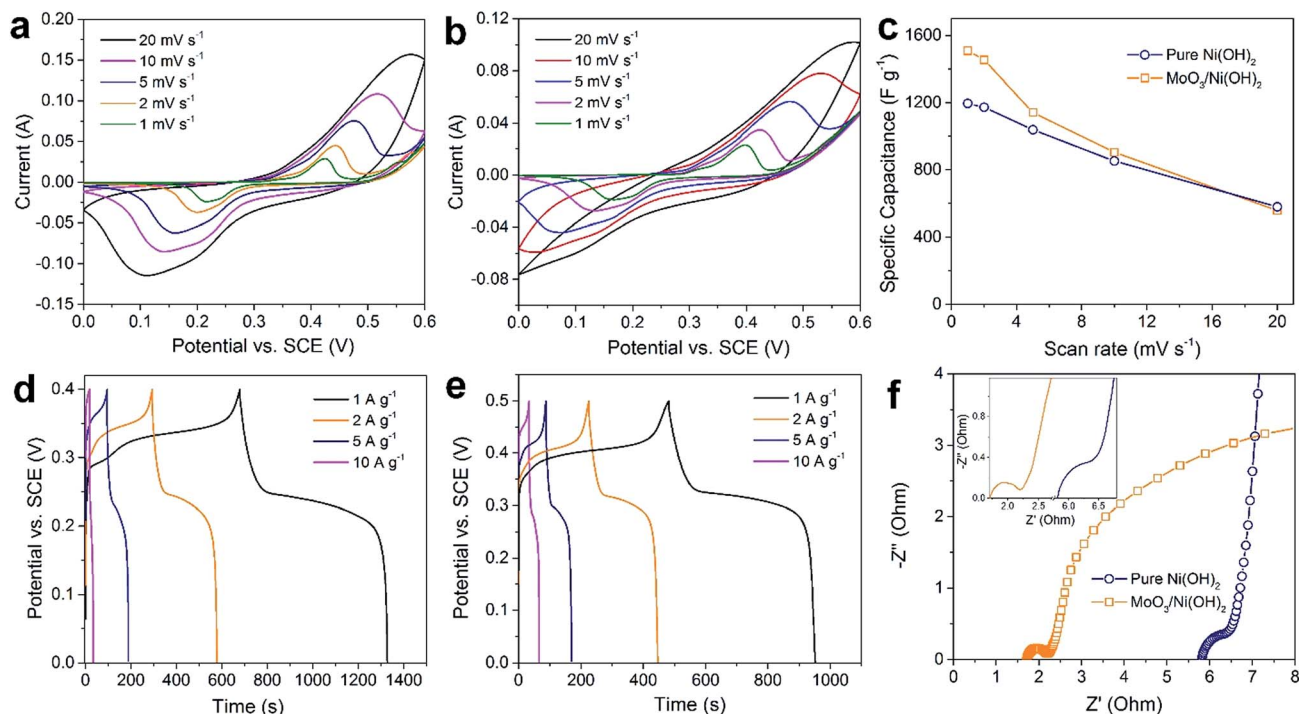
This journal is © The Royal Society of Chemistry 2017

J. Mater. Chem. A, 2017, **5**, 8343–8351 | 8347

Fig. 4 CV curves performed at different scan rates with the same voltage window of 0–0.6 V (*vs.* SCE) of (a) $MoO_3/Ni(OH)_2$ and (b) pure $Ni(OH)_2$ nanosheets. (c) Specific capacitances calculated from the corresponding different scan rates. GCD curves of (d) $MoO_3/Ni(OH)_2$ and (e) pure $Ni(OH)_2$ nanosheets obtained at different current densities from 1 to 10 A g^{-1}. (f) Nyquist plots of EIS for $MoO_3/Ni(OH)_2$ and pure $Ni(OH)_2$ nanosheets.

with hydrotalcite and constituents of hydroxyl-deficient host and interlayer species, such as anions and H_2O molecules.[41] The electrochromic reaction of $Ni(OH)_2$ is a reversible redox reaction in which the reduced form is nearly transparent while the oxidized material is dark brown, which is summarized in the following equation:[42,43]

$$[Ni(OH)_2 + OH^-]_{bleached} \leftrightarrow [NiOOH + H_2O + e^-]_{colored} \quad (3)$$

The as-prepared $MoO_3/Ni(OH)_2$ also exhibits electrochromic property due to the shell of α-$Ni(OH)_2$ nanosheets and the transmittance spectra of the sample coated on FTO glass recorded at ±1, 1.5 and 2 V are shown in Fig. 5a. The good reversibility of the bleaching/coloration and a stable transmittance change (ΔT) of 7.6, 13.5 and 26.1% for ±1, 1.5 and 2 V at a wavelength of 500 nm could be verified. Also, the bleaching/coloration responses occur almost instantaneously. Digital photographs of reversible bleached and colored states of the $MoO_3/Ni(OH)_2$ coating are shown in Fig. 5a, insets. The corresponding coloration efficiency is calculated to be 34.8 $cm^2 C^{-1}$ (Fig. 5b), which is comparable with that of $Ni(OH)_2$/ NiO reported previously.[43,44] This coloration phenomenon could be ascribed to the charge storage behavior of the electrode observed during the oxidation of the α-$Ni(OH)_2$ layer. It is also believed that the system can store charge by the conversion of α-$Ni(OH)_2$ into the NiOOH counterpart which finally acts as a color center for the respective electrochromic behavior.[45]

The electrochromism is shown to be driven by an as-prepared supercapacitor (Fig. S7†) which is a more efficient power source due to its high capacity, fast charging, and excellent cycling stability (Fig. 5c). An asymmetric supercapacitor cell, using a slurry of $MoO_3/Ni(OH)_2$ packed into full cells and CNTs as counter electrodes, was fabricated and then connected to power the electrochromic reaction on the FTO glass (Fig. 5d). The "Singapore Lion" pattern of $MoO_3/Ni(OH)_2$ was coated in advance. Notably, the pattern is almost transparent under the bleached state but discernibly displayed after being powered by the supercapacitor cell (Fig. 5e and S8†). The display evolved from a clear coated glass that allows high transmittance of the printed words to selective dark black patterned coloration. The corresponding transmittance spectra are shown in Fig. 5f, revealing a similar transmittance between the coated and bare FTO glass in the bleached state. Whereas in the colored state, a broad absorption band in the visible range and a corresponding transparency decrease from 80% to 56% at a wavelength of 500 nm were observed, making it a promising, inexpensive optical modulation material.

Given the electrochromic process happens when the charge injects or ejects, the electrochromic process can be integrated with charge storage devices.[14] Here we demonstrate the combination of electrochromism and energy storage, achieving the advantages of both in these two associated effects. The combination has two aspects (Fig. 6a). Firstly, the electrochromic device was made using 3 pieces of FTO glass coated with a thicker layer of $MoO_3/Ni(OH)_2$ and connected in order to
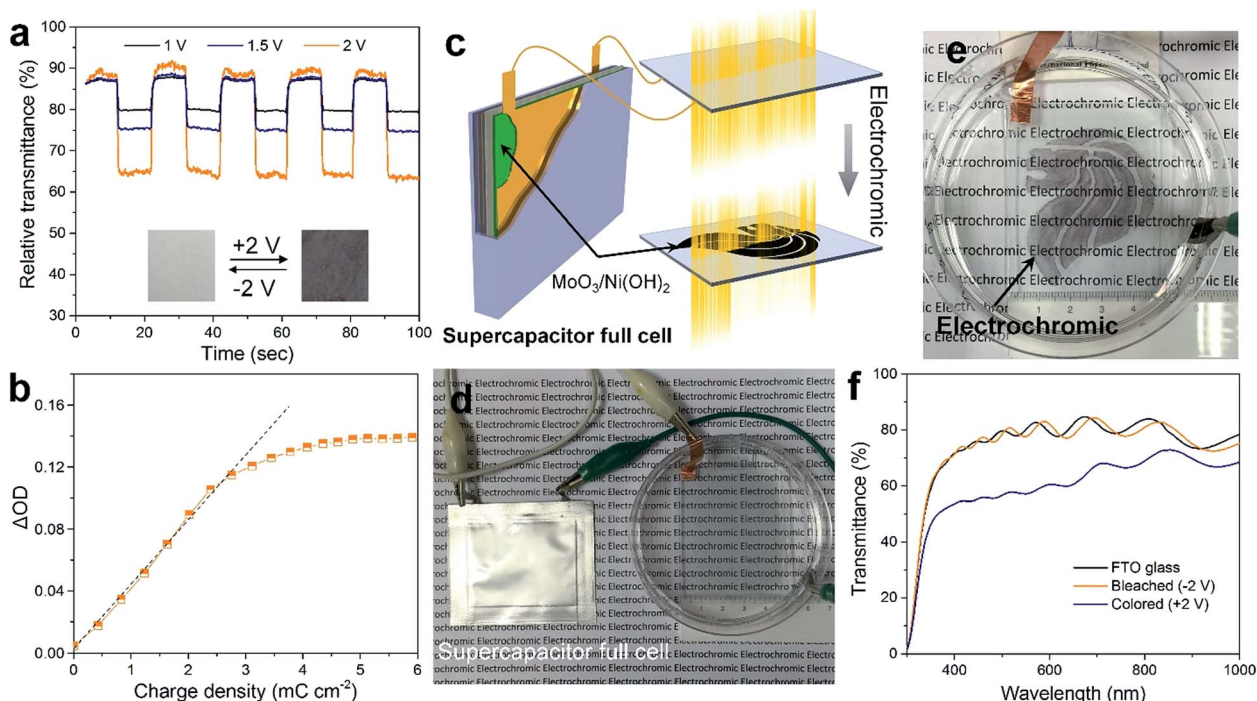
Fig. 5 (a) Transmittance spectra of coated FTO over five consecutive cycles of bleaching and coloration with ±1, 1.5 and 2 V biases. Insets are the corresponding photos of $MoO_3/Ni(OH)_2$/FTO glass under different conditions. (b) Optical density *vs.* charge density of $MoO_3/Ni(OH)_2$/FTO glass recorded at 500 nm. (c) Schematic diagram of electrochromic based on $MoO_3/Ni(OH)_2$/FTO glass powered by supercapacitor full cell. Photographs of FTO glass with "Singapore Lion" pattern of $MoO_3/Ni(OH)_2$ in (d) bleached and (e) colored states. (f) The corresponding transmittance spectra of the FTO glass and $MoO_3/Ni(OH)_2$/FTO glass electrode in bleached and colored states.

store enough energy for subsequent application (Fig. 6d). After applying a potential of +2 V, electrochromism took place and the glasses turned black (Fig. 6e). The corresponding

transmittance spectra in Fig. 6b show a transmittance level of 60% in the bleached state and 16% in the colored state. The transmittance contrast increased because of the higher loading
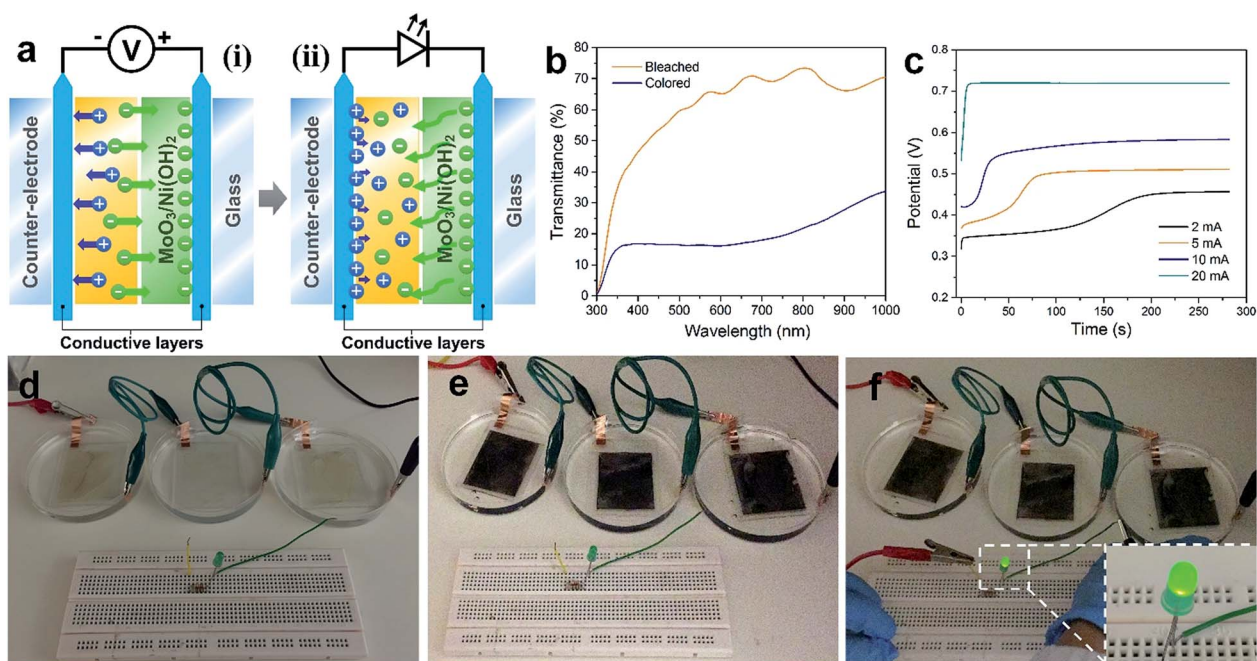
Fig. 6 (a) Schematic diagram of the electrochromic storage device. (b) Transmittance spectra of the coated FTO glass in the bleached and colored states. (c) Charging curves of a coated FTO glass at different current densities of 2, 5, 10 and 20 mA. (d–f) Photographs of electrochromic and charging processes. Inset is a photograph of a green LED lit by the electrochromic storage device.

of $MoO_3/Ni(OH)_2$. During the electrochromic reaction process, the charging performance of the $MoO_3/Ni(OH)_2$/FTO glass was investigated at different current densities of 2, 5, 10 and 20 mA. A higher current density leads to a faster charging rate and higher resultant voltage, as shown in Fig. 6c. Thereafter, the energy stored in the electrochromic devices was utilized. The three charged electrochromic FTO substrates are connected in series to form a closed circuit to power an LED (Fig. 6f). The electrochromic device could easily light up a commercial green LED after being charged (Fig. 6f, inset). Our newly designed 2D-on-2D architecture not only has a good electrochromic property, but also features further energy storage properties, which may be used to power electronic devices, such as mobile phones and sensors, in the future.

Conclusions

In summary, dissimilar 2D-on-2D hierarchical architecture of nanobelt core–nanosheets shell of disparate transition metal composite based on a facile solution processing method was produced. The growth of 2D $Ni(OH)_2$ nanosheets on free-standing 2D MoO_3 nanobelts manifests in a 3D hierarchical architecture of numerous nanosheets that extend radially outward. Moreover, bifunctional electrochromism–super-capacitive properties are simultaneously realized based on the inexpensive electrochemical active transition metal hydroxide hierarchical structure. The porous core–shell nanostructures of $Ni(OH)_2/MoO_3$ display desirable electrochromic optical modulation and coloration efficiency properties alongside favorable pseudocapacitive storage and specific capacitance properties. Such an integrated energy system is anticipated to have a broad range of smart applications in buildings, automobiles and other various electronics needs.

Acknowledgements

References

1 X. Yu, T. J. Marks and A. Facchetti, *Nat. Mater.*, 2016, **15**, 383.

2 N. E. Motl, A. F. Smith, C. J. DeSantisa and S. E. Skrabalak, *Chem. Soc. Rev.*, 2014, **43**, 3823.

3 P. Yang, Y. Ding, Z. Lin, Z. Chen, Y. Li, P. Qiang, M. Ebrahimi, W. Mai, C. P. Wong and Z. L. Wang, *Nano Lett.*, 2014, **14**, 731.

4 H.-Y. Wang, S.-F. Hung, H.-Y. Chen, T.-S. Chan, H. M. Chen and B. Liu, *J. Am. Chem. Soc.*, 2016, **138**, 36.

5 C.-W. Tung, Y.-Y. Hsu, Y.-P. Shen, Y. Zheng, T.-S. Chan, H.-S. Sheu, Y.-C. Cheng and H. M. Chen, *Nat. Commun.*, 2015, **6**, 8106.

6 M. Gao, L. Zhu, W. L. Ong, J. Wang and G. W. Ho, *Catal. Sci. Technol.*, 2015, **5**, 4703.

7 L. Zhu, M. Hong and G. W. Ho, *Sci. Rep.*, 2015, **5**, 11609.

8 T. Zhu, C. K. N. Peh, M. Hong and G. W. Ho, *Chem.–Eur. J.*, 2014, **20**, 11505.

9 Z. Sun, T. Liao, Y. Dou, S. M. Hwang, M. S. Park, L. Jiang, J. H. Kim and S. X. Dou, *Nat. Commun.*, 2014, **5**, 3813.

10 M. Chhetri, M. Rana, B. Loukya, P. K. Patil, R. Datta and U. K. Gautam, *Adv. Mater.*, 2015, **27**, 4430.

11 B. Wang, J. S. Chen, Z. Wang, S. Madhavi and X. W. Lou, *Adv. Energy Mater.*, 2012, **2**, 1188.

12 H. Yin, S. Zhao, K. Zhao, A. Muqsit, H. Tang, L. Chang, H. Zhao, Y. Gao and Z. Tang, *Nat. Commun.*, 2015, **6**, 6430.

13 N.-T. Suen, S.-F. Hung, Q. Quan, N. Zhang, Y.-J. Xu and H. M. Chen, *Chem. Soc. Rev.*, 2017, **46**, 337.

14 P. Yang, P. Sun and W. Mai, *Mater. Today*, 2015, **19**, 394.

15 P. Yang, P. Sun, Z. Chai, L. Huang, X. Cai, S. Tan, J. Song and W. Mai, *Angew. Chem., Int. Ed.*, 2014, **53**, 11935.

16 J. W. Liu, J. Zheng, J. L. Wang, J. Xu, H. H. Li and S. H. Yu, *Nano Lett.*, 2013, **13**, 3589.

17 R. T. Wen, C. G. Granqvist and G. A. Niklasson, *Nat. Mater.*, 2015, **14**, 996.

18 L. Guo, Y. Ren, J. Liu, S. Y. Chiam and W. K. Chim, *Small*, 2014, **10**, 2611.

19 D. Wei, M. R. J. Scherer, C. Bower, P. Andrew, T. Ryhänen and U. Steiner, *Nano Lett.*, 2012, **12**, 1857.

20 S. Jin, G. Yang, H. Song, H. Cui and C. Wang, *ACS Appl. Mater. Interfaces*, 2015, **7**, 24932.

21 Y. Shen, Y. Yang, F. Hu, Y. Xiao, P. Yan and Z. Li, *Mater. Sci. Semicond. Process.*, 2015, **29**, 250.

22 J. Zhu, L. Huang, Y. Xiao, L. Shen, Q. Chen and W. Shi, *Nanoscale*, 2014, **6**, 6772.

23 D. Chen, M. Liu, L. Yin, T. Li, Z. Yang, X. Li, B. Fan, H. Wang, R. Zhang, Z. Li and H. Xu, *J. Mater. Chem.*, 2011, **21**, 9332.

24 P. J. Lu, M. Lei and J. Liu, *CrystEngComm*, 2014, **16**, 6745.

25 Y. B. Li, Y. Bando, D. Golberg and K. Kurashima, *Appl. Phys. Lett.*, 2002, **81**, 5048.

26 Z. Wang, S. Madhavi and X. W. Lou, *J. Phys. Chem. C*, 2012, **116**, 12508.

27 K. Dewangan, N. N. Sinha, P. K. Sharma, A. C. Pandey, N. Munichandraiah and N. S. Gajbhiye, *CrystEngComm*, 2011, **13**, 927.

28 W. Zhou, X. Liu, Y. Sang, Z. Zhao, K. Zhou, H. Liu and S. Chen, *ACS Appl. Mater. Interfaces*, 2014, **6**, 4578.

29 L. Zheng, Y. Xu, D. Jin and Y. Xie, *Chem. Mater.*, 2009, **21**, 5681.

30 R. Li, Z. Hu, X. Shao, P. Cheng, S. Li, W. Yu, W. Lin and D. Yuan, *Sci. Rep.*, 2016, **6**, 18737.

31 K. Zhou, W. Zhou, L. Yang, J. Lu, S. Cheng, W. Mai, Z. Tang, L. Li and S. Chen, *Adv. Funct. Mater.*, 2015, **25**, 7530.

32 M. Ayala-G, E. Puello, P. Quintana, G. González-García and C. Diaz, *RSC Adv.*, 2015, **5**, 102652.

33 H. Y. Chen, H. C. Su, C. H. Chen, K. L. Liu, C. M. Tsai, S. J. Yen and T. R. Yew, *J. Mater. Chem.*, 2011, **21**, 5745.

34 I. Chang, T. T. Chen, M. H. Yang, H. T. Chiu and C. Y. Lee, *J. Mater. Chem. A*, 2014, **2**, 10370.

35 C. Tang, N. Cheng, Z. Pu, W. Xing and X. Sun, *Angew. Chem., Int. Ed.*, 2015, **54**, 9351.

36 L. Zhang, Q. Ding, Y. Huang, H. Gu, Y. E. Miao and T. Liu, *ACS Appl. Mater. Interfaces*, 2015, **7**, 22669.

37 H. B. Li, M. H. Yu, F. X. Wang, P. Liu, Y. Liang, J. Xiao, C. X. Wang, Y. X. Tong and G. W. Yang, *Nat. Commun.*, 2013, **4**, 1894.

38 Y. Zhao, L. Hu, S. Zhao and L. Wu, *Adv. Funct. Mater.*, 2016, **26**, 4085.

39 T. Zhu, J. Wang and G. W. Ho, *Nano Energy*, 2015, **18**, 273.

40 R. Zhang, Y. Xu, D. Harrison, J. Fyson and D. Southee, *Int. J. Electrochem. Sci.*, 2016, **11**, 7922.

41 T. Gao and B. P. Jelle, *J. Phys. Chem. C*, 2013, **117**, 17294.

42 W. L. Ong, S. W. L. Ng, C. Zhang, M. Hong and G. W. Ho, *J. Mater. Chem. A*, 2016, **4**, 13307.

43 F. Grote, Z. Y. Yu, J. L. Wang, S. H. Yu and Y. Lei, *Small*, 2015, **11**, 4666.

44 X. H. Xia, J. P. Tu, J. Zhang, X. L. Wang, W. K. Zhang and H. Huang, *Sol. Energy Mater. Sol. Cells*, 2008, **92**, 628.

45 D. K. Bora, A. Braun, R. Erni, U. Müller, M. Döbelie and E. C. Constable, *Phys. Chem. Chem. Phys.*, 2013, **15**, 12648.